molecules

MDPI

*Article*

# Elucidating the Role of Surface $Ce^{4+}$ and Oxygen Vacancies of $CeO_2$ in the Direct Synthesis of Dimethyl Carbonate from $CO_2$ and Methanol

**Guoqiang Zhang [1,*], Yuan Zhou [1,2], Yanlin Yang [1], Tiantian Kong [1], Ya Song [1], Song Zhang [1] and Huayan Zheng [1,*]**

[1] Department of Food Science and Engineering, Moutai Institute, Renhuai 564502, China
[2] Experimental Training Teaching Center, Moutai Institute, Renhuai 564502, China
* Correspondence: zgq198615@163.com (G.Z.); andyzheng1109@163.com (H.Z.)

**Abstract:** Cerium dioxide ($CeO_2$) was pretreated with reduction and reoxidation under different conditions in order to elucidate the role of surface $Ce^{4+}$ and oxygen vacancies in the catalytic activity for direct synthesis of dimethyl carbonate (DMC) from $CO_2$ and methanol. The corresponding catalysts were comprehensively characterized using $N_2$ physisorption, XRD, TEM, XPS, TPD, and $CO_2$-FTIR. The results indicated that reduction treatment promotes the conversion of $Ce^{4+}$ to $Ce^{3+}$ and improves the concentration of surface oxygen vacancies, while reoxidation treatment facilitates the conversion of $Ce^{3+}$ to $Ce^{4+}$ and decreases the concentration of surface oxygen vacancies. The catalytic activity was linear with the number of moderate acidic/basic sites. The surface $Ce^{4+}$ rather than oxygen vacancies, as Lewis acid sites, promoted the adsorption of $CO_2$ and the formation of active bidentate carbonates. The number of moderate basic sites and the catalytic activity were positively correlated with the surface concentration of $Ce^{4+}$ but negatively correlated with the surface concentration of oxygen vacancies. The surface $Ce^{4+}$ and lattice oxygen were active Lewis acid and base sites respectively for $CeO_2$ catalyst, while surface oxygen vacancy and lattice oxygen were active Lewis acid and base sites, respectively, for metal-doped $CeO_2$ catalysts. This may result from the different natures of oxygen vacancies in $CeO_2$ and metal-doped $CeO_2$ catalysts.

**Keywords:** carbon dioxide; dimethyl carbonate; $CeO_2$; oxygen vacancy; lattice oxygen

check for updates

**Citation:** Zhang, G.; Zhou, Y.; Yang, Y.; Kong, T.; Song, Y.; Zhang, S.; Zheng, H. Elucidating the Role of Surface $Ce^{4+}$ and Oxygen Vacancies of $CeO_2$ in the Direct Synthesis of Dimethyl Carbonate from $CO_2$ and Methanol. *Molecules* **2023**, *28*, 3785. https://doi.org/10.3390/molecules28093785

Academic Editor: Alessandra Puglisi

Received: 8 March 2023
Revised: 19 April 2023
Accepted: 26 April 2023
Published: 28 April 2023

**Copyright:** © 2023 by the authors. Licensee MDPI, Basel, Switzerland. This article is an open access article distributed under the terms and conditions of the Creative Commons Attribution (CC BY) license (https://creativecommons.org/licenses/by/4.0/).

## 1. Introduction

The emission of $CO_2$ into the earth's atmosphere is continuously increasing with the growing burning of fossil fuels and industrial activities. For example, about 33,890.80 million tons of $CO_2$ was emitted into the atmosphere in 2018. The global $CO_2$ concentration in the atmosphere reached 407.65 ppm in September 2019, which is about 1.2 times as high as that of the past 40 years [1]. According to the earth's $CO_2$, the concentration of $CO_2$ further increased to 416.47 ppm on 30 May 2020 [2]. The dramatically increased $CO_2$ emission results in severe climate change, which brings about a series of issues in terms of ecology, economy, and the environment. Taking these facts into consideration, it is necessary to develop effective approaches to mitigate $CO_2$ emission.

As an important part of carbon dioxide capture, utilization, and storage (CCUS), the chemical transformation of $CO_2$ to fuels and value-added chemicals can not only alleviate $CO_2$ emission but also reduce the dependence on fossil resources, which is of great significance for the sustainable development of energy, the environment, and the economy. Dimethyl carbonate (DMC), as one of the downstream products of methanol, is considered a green chemical, which has been widely applied as an intermediate for organic synthesis, an electrolyte for lithium-ion batteries, and a raw material for the synthesis of polycarbonate [3]. Among various synthesis approaches, the direct synthesis of DMC from

$CO_2$ and methanol is deemed a green route due to the beneficial environment impact and high atomic use [4].

Although this reaction suffers from low DMC yield due to the thermodynamic limit, a significant endeavor has been made to develop effective catalysts, such as supported catalysts, alkali carbonate catalysts, ionic liquid catalysts, heteropoly acid catalysts, and transition metal oxide catalysts [4,5]. Transition metal oxides, especially $ZrO_2$ and $CeO_2$, have attracted tremendous attention in recent years due to their promising catalytic activity. Fujimoto et al. [6] first reported that $ZrO_2$ can catalyze $CO_2$ and methanol to DMC, and the catalytic activity was closely related to the surface basic and acidic sites.

Bell et al. [7] further studied the reaction mechanism over $ZrO_2$ using in situ infrared spectra. The results revealed that surface coordinately unsaturated $Zr^{4+}$ cations, such as Lewis acid sites, promote the dissociation of methanol to methoxide ($–OCH_3$) and a proton, which can react with the surface hydroxyl group to produce water. Next, bidentate carbonates were formed by the interaction of C and O atoms in $CO_2$ with surface Lewis acid–base pairs ($Zr^{4+}$–$O^{2-}$), which were subsequently inserted into $–OCH_3$ and formed monodentate methyl carbonate (MMC) intermediate species. Finally, the MMC species reacted with methyl ($–CH_3$) from the dissociation of methanol on Lewis base sites ($O^{2-}$) to produce DMC [7]. In this regard, the improvement of surface acidic and basic sites is beneficial for the catalytic activity. For example, Xiao et al. [8] found that the doping of Fe into $ZrO_2$ can significantly improve the surface acidic and basic sites, and the catalytic activity was positively correlated with surface acidic and basic sites.

Compared with $ZrO_2$, $CeO_2$ shows much higher catalytic activity and thus receives much more attention. For example, Marin et al. [9] studied the kinetic and reaction mechanism over a $CeO_2$ catalyst, and the results showed that the reaction follows the Langmuir–Hinshelwood mechanism, in which the adsorption of $CO_2$ is considered the rate-determining step. Wang et al. [10] reported that the catalytic activity of $CeO_2$ is closely related to the corresponding morphology, and $CeO_2$ nanorods showed much higher catalytic activity than that of the cube and octahedron due to the exposure of more acidic and basic sites. A further study of the morphology effect was performed with in situ infrared spectra. The results indicated that the (110) facet of $CeO_2$ nanorods promotes the formation of bidentate carbonates that can react with $–OCH_3$ to form MMC. However, other carbonates, such as monodentate carbonates, bicarbonates, and bridged carbonates, cannot accomplish that process, and therefore, the bidentate carbonates were identified as active species in terms of $CO_2$ adsorption [11]. In addition, doping the metal cation of $Ca^{2+}$ [12], $Zn^{2+}$ [13,14], $Mn^{2+}$ [15], $Ti^{4+}$ [16], $Fe^{3+}$ [17], $Co^{4+}$ [18], and $Zr^{4+}$ [19,20] into the lattice of $CeO_2$ promotes the formation of oxygen vacancies ($O_V$) and is also proven to be an efficient strategy to improve catalytic activity. The results of in situ infrared spectra over the Zr–$CeO_2$ catalyst demonstrated that $O_V$ promote the formation of bidentate carbonates via the interaction of C and O atoms in $CO_2$ with surface Lewis acid–base pairs ($O_V$–$O^{2-}$), in which one of the O atoms in $CO_2$ is inserted into $O_V$ [19]. Therefore, both the amount of adsorbed $CO_2$ and the catalytic activity increase with the increasing concentration of $O_V$ [12–20].

It is obvious that two different Lewis acid–base pairs, $Zr^{4+}$–$O^{2-}$ and $O_V$–$O^{2-}$, are considered active sites in $ZrO_2$ and metal-doped $CeO_2$ catalysts, respectively. However, of $Ce^{4+}$ and $O_V$, which one is catalytically active in $CeO_2$ catalysts? Is the formation of $O_V$ in $CeO_2$ catalysts beneficial to the catalytic activity as in metal-doped $CeO_2$ catalysts? The answers to these two questions are of prominent significance to the design of an effective catalyst. Inspired by this, the surface concentrations of $Ce^{4+}$ and $O_V$ were regulated via reduction and reoxidation of $CeO_2$ under different conditions in this work. Combining XRD, TEM, XPS, $CO_2$-TPD, $NH_3$-TPD, and $CO_2$-FTIR results, the role of surface $Ce^{4+}$ and $O_V$ in the adsorption of $CO_2$ and the catalytic activity for DMC synthesis from $CO_2$ and methanol were deeply elucidated. The possible influence of two types of $O_V$ on the adsorption and activation of $CO_2$ was also proposed.

## 2. Results

### *2.1. Textural Properties of Catalysts*

The $N_2$ adsorption–desorption isotherms of $CeO_2$ treated under different conditions are shown in Figure 1. All the samples showed the type IV isotherm with a distinct hysteresis loop, indicating the presence of a mesopore.

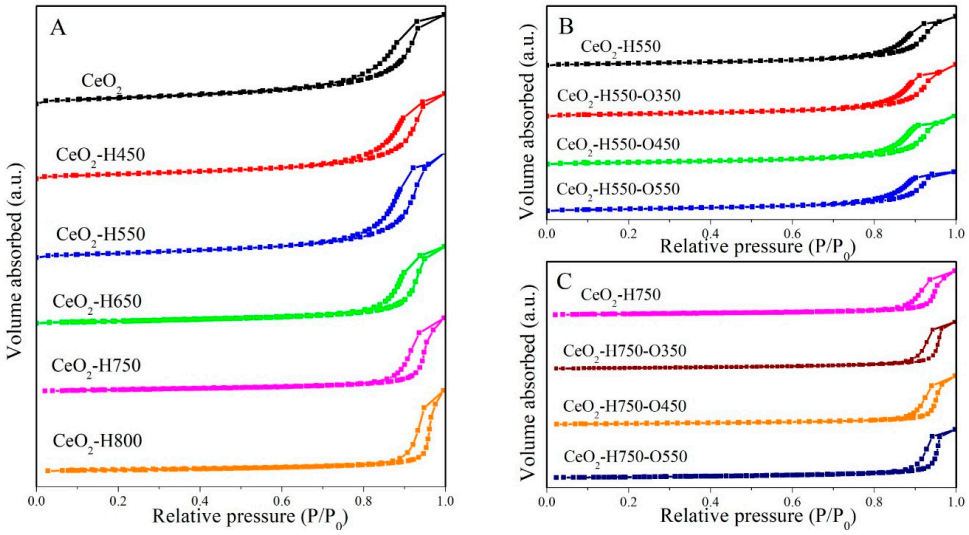



**Figure 1.** $N_2$ adsorption–desorption isotherms of catalysts (**A**) $CeO_2$ reduced at different temperatures, (**B**) $CeO_2$–H550 reoxidized at different temperatures, and (**C**) $CeO_2$–H750 reoxidized at different temperatures.

The detailed texture parameters are listed in Table 1. As seen in Table 1, the specific surface area and pore volume of $CeO_2$ gradually decreased with an increase in the reduction temperature; however, the pore size of $CeO_2$ presented the opposite trend, which suggests that the mesopore originated from the piled pore. This phenomenon may arise from the aggregation of $CeO_2$ particles induced by high temperature [21]. In contrast, as $CeO_2$–H550 and $CeO_2$–H750 were reoxidized under an air atmosphere at 350 °C, 450 °C, and 550 °C, the texture parameters did not change so much.

**Table 1.** Textural parameters of catalysts.

| Catalysts | $S_{BET}$ ($m^2 \cdot g^{-1}$) | $V_p$ ($cm^3/g$) | Pore Size (nm) |
|---|---|---|---|
| $CeO_2$ | 130.3 | 0.65 | 13.8 |
| $CeO_2$–H450 | 120.9 | 0.59 | 14.6 |
| $CeO_2$–H550 | 106.2 | 0.57 | 14.6 |
| $CeO_2$–H650 | 72.9 | 0.47 | 16.9 |
| $CeO_2$–H750 | 28.2 | 0.27 | 23.1 |
| $CeO_2$–H800 | 18.6 | 0.24 | 30.7 |
| $CeO_2$–H550–O350 | 107.3 | 0.59 | 14.8 |
| $CeO_2$–H550–O450 | 109.2 | 0.64 | 14.9 |
| $CeO_2$–H550–O550 | 107.8 | 0.52 | 12.3 |
| $CeO_2$–H750–O350 | 23.1 | 0.23 | 25.1 |
| $CeO_2$–H750–O450 | 26.2 | 0.27 | 25.6 |
| $CeO_2$–H750–O550 | 24.5 | 0.24 | 23.9 |

### *2.2. XRD Analysis of Catalysts*

XRD characterization was performed to analyze the crystal structure of $CeO_2$, and the results are presented in Figure 2. All the samples displayed the characteristic diffraction peaks of a cubic fluorite structure (JCPDS no. 65-5923), and the peaks at 28.5°, 33.0°, 47.5°,

56.5°, 59.4°, and 69.6° were ascribed to the (111), (200), (220), (311), (222), and (400) crystal facets of $CeO_2$, respectively [19].

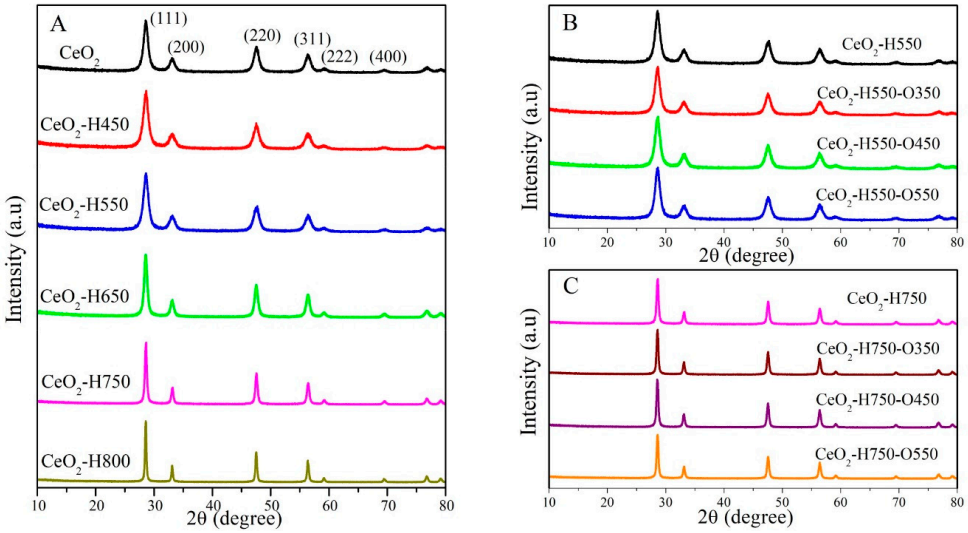



**Figure 2.** XRD patterns of catalysts (**A**) $CeO_2$ reduced at different temperatures, (**B**) $CeO_2$–H550 reoxidized at different temperatures, and (**C**) $CeO_2$–H750 reoxidized at different temperatures.

As seen in Figure 2A, the intensity and width of the characteristic diffraction peaks of $CeO_2$ did not change obviously as the reduction temperature decreased below 550 °C, indicating the similar crystal size of $CeO_2$, $CeO_2$–H450, and $CeO_2$–H550. However, as the reduction temperature increased beyond 550 °C, the peak intensity was gradually enhanced and the peak width gradually narrowed, indicating the gradually increasing crystal size. The crystal size of each catalyst is presented in Table 2, which was calculated using the Scherrer equation as follows: $D = K\lambda/[(\beta - b)\cos\theta]$, where $K$ is the Scherrer constant (0.89), $\lambda$ is 0.15414 nm (the wavelength of Cu K$\alpha$ radiation), $\beta$ is the full width at half-maximum of the $CeO_2$(111) diffraction peak, $b$ is the corrected full width at half-maximum of the instrument, and $\theta$ is the diffraction angle [22].

**Table 2.** Crystal and particle size of catalysts.

| Catalysts | $d_{CeO_2}$ (nm) [a] | Catalysts | $d_{CeO_2}$ (nm) [a] |
|---|---|---|---|
| $CeO_2$ | 7.1 | $CeO_2$–H550–O350 | 7.6 |
| $CeO_2$–H450 | 7.4 | $CeO_2$–H550–O450 | 7.3 |
| $CeO_2$–H550 | 7.4 | $CeO_2$–H550–O550 | 7.5 |
| $CeO_2$–H650 | 12.9 | $CeO_2$–H750–O350 | 32.1 |
| $CeO_2$–H750 | 25.5 | $CeO_2$–H750–O450 | 29.7 |
| $CeO_2$–H800 | 46.6 | $CeO_2$–H750–O550 | 31.6 |

[a] Crystal size calculated from the XRD diffraction peaks of $CeO_2$ (111) based on the Scherrer equation.

As seen in Table 2, similar crystal sizes of about 7~8 nm were observed for $CeO_2$, $CeO_2$–H450, and $CeO_2$–H550. However, the crystal sizes significantly increased from 7.4 to 46.6 nm with an increase in the reduction temperature from 550 °C to 800 °C, which resulted from the aggregation of $CeO_2$ particles [21,23,24]. In addition, the crystal sizes of $CeO_2$–H550 remained basically about 7~8 nm after reoxidation treatment, while those of $CeO_2$–H750 remained basically about 30 nm after reoxidation treatment. These results revealed that reoxidation treatment does not obviously affect the crystal sizes of $CeO_2$.

### *2.3. TEM of Catalysts*

TEM was used to characterize the morphology of catalysts. As seen in Figure 3, the morphology of catalysts was irregular, including being polyhedron- and rodlike. The

particle size of $CeO_2$, $CeO_2$–H450, $CeO_2$–H550, $CeO_2$–H550–O350, $CeO_2$–H550–O450, and $CeO_2$–H550–O550 seemed almost the same. The possible reason may be that the starting material of $CeO_2$ was already calcinated at 550 °C for 5 h in a muffle furnace before reduction and reoxidation treatment. However, the particles significantly aggregated with increasing reduction temperature as the reduction temperature increased beyond 550 °C. In addition, reoxidation treatment did not obviously affect the particle sizes of the catalysts. This was consistent with the results of XRD.

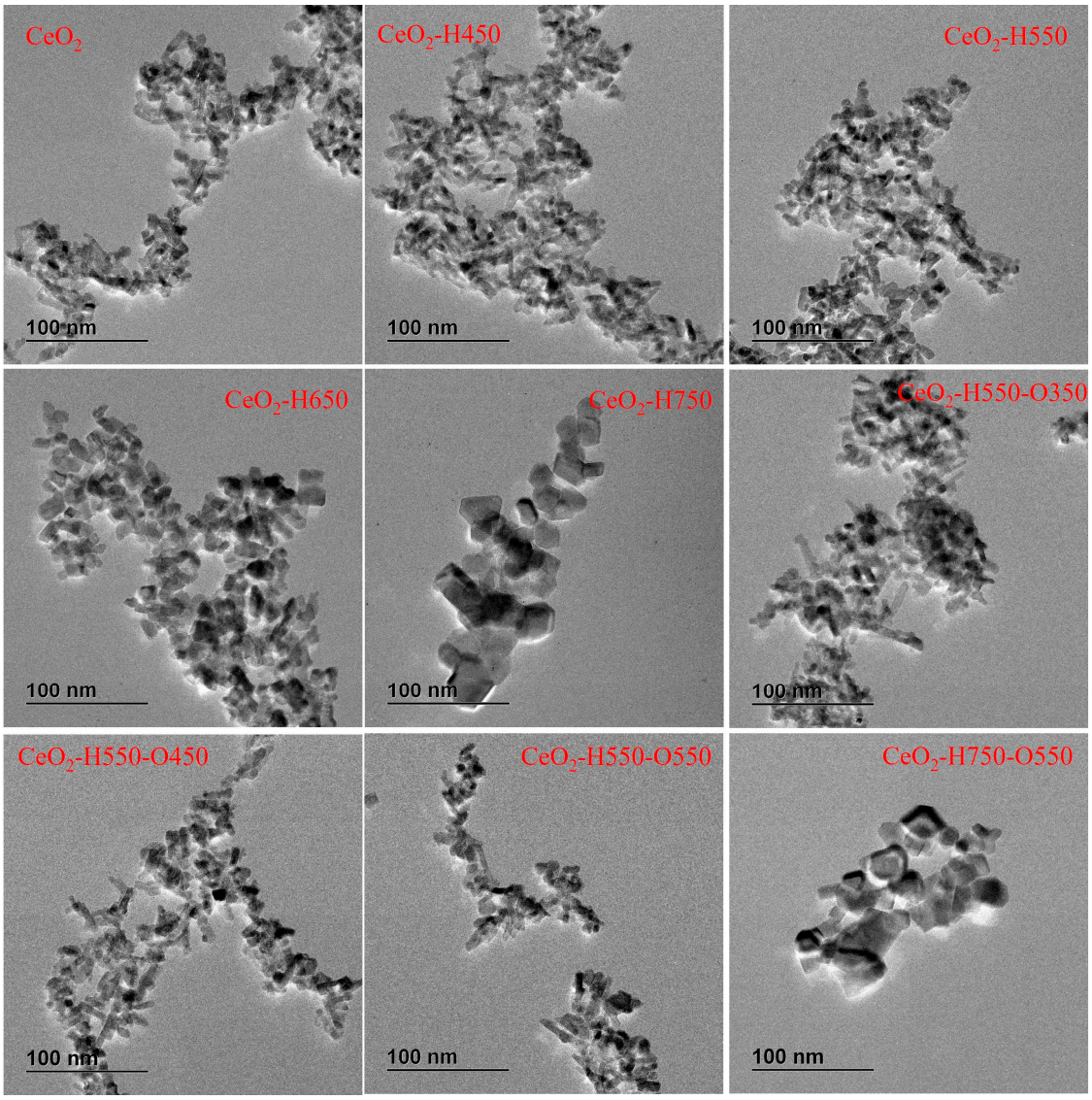



**Figure 3.** Representative TEM images of catalysts.

HRTEM was used to further characterize the exposed facet of catalysts, as shown in Figure 4. The observed lattice fringes of about 0.31 and 0.27 nm corresponded to the (111) and (200) facets of $CeO_2$. Obviously, the main exposed facet was (111), and the (200) facet only appeared in $CeO_2$–H650 and $CeO_2$–H750–O550, which was in line with our previous studies [15,19]. These results also indicated that the reduction temperature and reoxidation treatment do not apparently affect the exposed facet of catalysts.

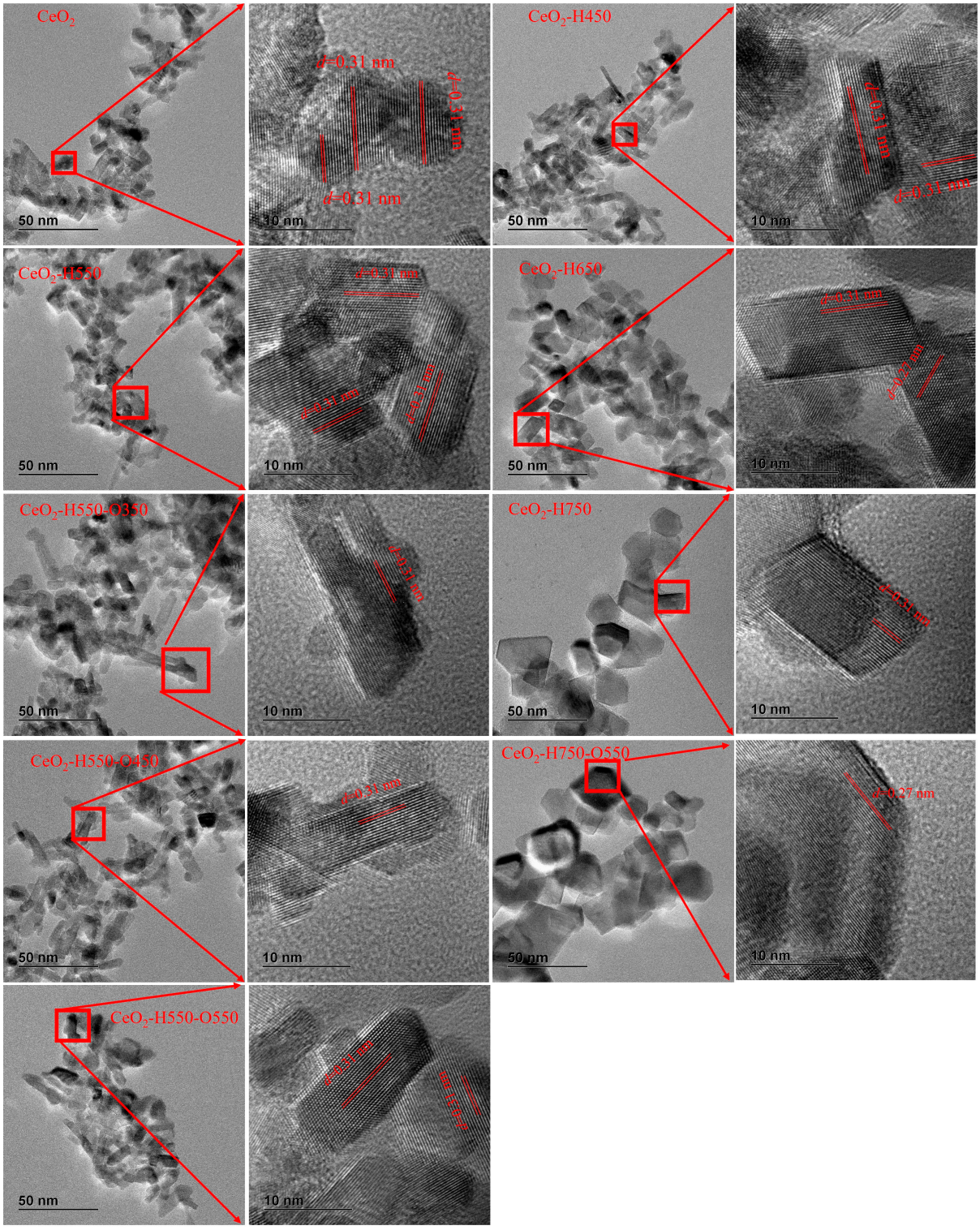



**Figure 4.** Representative HRTEM images of catalysts.

### *2.4. Surface Composition Analysis of Catalysts*

XPS characterization was performed to analyze the chemical state of the surface Ce and O of catalysts, as shown in Figure 5. After gaussian fitting, the Ce 3D spectra could be fitted into eight peaks: U′′′(~916.3 eV), U′′(~907.4 eV), U′(~903.3 eV), U(~900.6 eV), V′′′(~898.0 eV), V′′(~888.4 eV), V′(~884.9 eV), and V(~882.1 eV) [16].

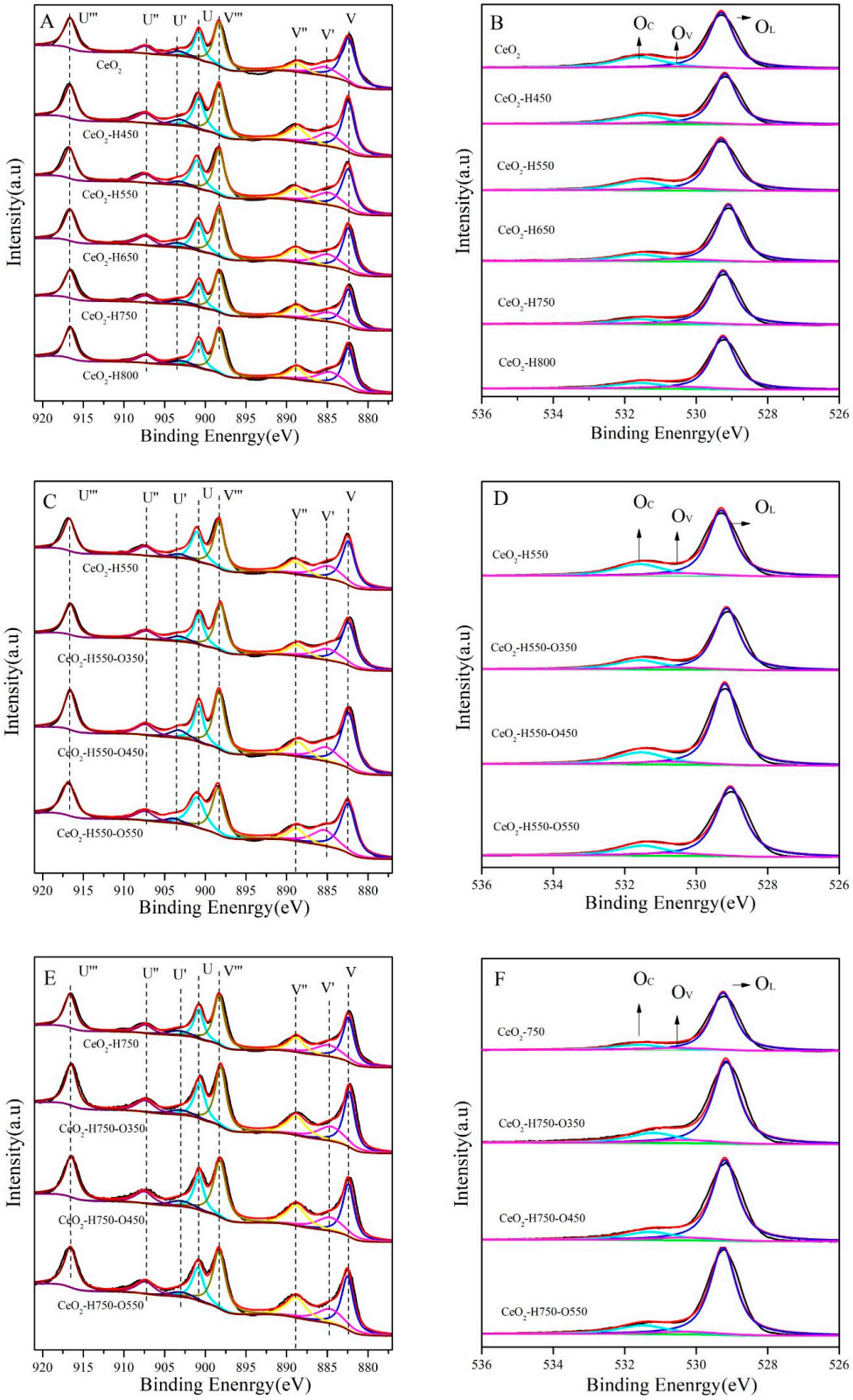



**Figure 5.** Ce 3d (**A**) and O 1s (**B**) XPS spectra of $CeO_2$ reduced at different temperatures, Ce 3d (**C**) and O 1s (**D**) XPS spectra of $CeO_2$–H550 reoxidized at different temperatures, and Ce 3d (**E**) and O 1s (**F**) XPS spectra of $CeO_2$–H750 reoxidized at different temperatures.

In the O 1s spectra, the peaks at ~529.0 eV, ~530.5 eV, and ~531.5 eV were assigned to the surface lattice oxygen ($O_L$), oxygen vacancies ($O_V$), and chemisorbed oxygen species

($O_C$), respectively [25,26]. The surface concentration of $O_V$ was calculated based on the peak area from gaussian fitting, and the results are listed in Table 3.

**Table 3.** Surface concentration of Ce cations and oxygen vacancies determined with XPS.

| Catalysts | Ce Atom Ratio (%) | | O Atom Ratio (%) |
|---|---|---|---|
| | $Ce^{3+}$ | $Ce^{4+}$ | $O_V$ |
| $CeO_2$ | 13.5 | 86.5 | 5.3 |
| $CeO_2$–H450 | 15.7 | 84.3 | 6.9 |
| $CeO_2$–H550 | 16.2 | 83.8 | 7.6 |
| $CeO_2$–H650 | 16.7 | 83.3 | 7.8 |
| $CeO_2$–H750 | 16.8 | 83.2 | 8.1 |
| $CeO_2$–H800 | 17.7 | 82.3 | 8.5 |
| $CeO_2$–H550–O350 | 15.7 | 84.3 | 7.1 |
| $CeO_2$–H550–O450 | 15.3 | 84.7 | 6.6 |
| $CeO_2$–H550–O550 | 15.2 | 84.8 | 6.7 |
| $CeO_2$–H750–O350 | 15.8 | 84.2 | 7.2 |
| $CeO_2$–H750–O450 | 15.2 | 84.8 | 6.5 |
| $CeO_2$–H750–O550 | 14.9 | 85.1 | 6.1 |

As seen in Table 3, the concentration of $Ce^{3+}$ gradually increased from 13.5 to 17.7% as the reduction temperature increased to 800 °C, while that of $Ce^{4+}$ gradually decreased from 86.5 to 82.3%. Moreover, the concentration of $O_V$ also increased with an increase in the reduction temperature. These results were consistent with the work reported by our group and Chen et al. that the percentage of $Ce^{3+}$ is positively correlated with that of $O_V$ [16,19]. In addition, the concentrations of $Ce^{3+}$ and $O_V$ decreased for $CeO_2$–H550 and $CeO_2$–H750 after reoxidation treatment.

The concentration of the surface $O_V$ of $CeO_2$ is closely related to the calcination atmosphere, oxygen partial pressure, and calcination temperature [27]. The formation of $O_V$ is accomplished through the diffusion of lattice oxygen to the environment, where the content of oxygen is low. Under these circumstances, an oxygen vacancy is a kind of anionic defect. When $CeO_2$ was exposed to the reductive $H_2$ atmosphere, the lattice oxygen reacted with $H_2$ and formed $H_2O$ and therefore promoted the formation of $O_V$; moreover, the promoting effect gradually strengthened with increasing reduction temperature. It should be noted that two surplus electrons would be retained in the crystal structure of $CeO_2$ accompanied with the formation of $O_V$, and the two surplus electrons can bind with two adjacent $Ce^{4+}$, resulting in the conversion of $Ce^{4+}$ to $Ce^{3+}$. Moreover, the two electrons were mobile that could migrate between two adjacent Ce ions. In other words, the two quasi-free mobile electrons were trapped around the anionic defect ($O_V$), which could migrate between adjacent Ce ions and cause electron conduction. A material with this kind of defect is an N-type semiconductor [28]. The O atoms were reinserted back into $O_V$ and formed $O_L$ when $CeO_2$–H550 and $CeO_2$–H750 were reoxidized under an air atmosphere. In this process, the trapped electrons around $O_V$ were transferred to O atoms, and the conversion of $Ce^{3+}$ to $Ce^{4+}$ occurred simultaneously. Singhal et al. [29] also found that the conversion between $O_V$ and $O_L$ is reversible to some extent.

Furthermore, as shown in Figure S1, the color of $CeO_2$ gradually changed from yellow to brown and finally to gray-black with the increase in the reduction temperature, and the color changed back to yellow to a certain degree when $CeO_2$–H550 and $CeO_2$–H750 were reoxidized under an air atmosphere. This is because the trapped electrons around $O_V$ can absorb light with a certain wavelength and the absorption capacity is gradually enhanced with the increasing number of electrons or $O_V$ [21,29]. This result also indicated that reduction treatment is favorable for the formation of $O_V$, while reoxidation treatment plays the opposite role.

### *2.5. Surface Acidity and Basicity Analysis of Catalysts*

The surface acidity and basicity of catalysts were characterized using $NH_3$-TPD and $CO_2$-TPD, as shown in Figures 6 and 7, and the detailed results are listed in Table 4. The desorption peaks in the temperature region of 50~200, 200~400, and 400~600 °C in $CO_2$-TPD and $NH_3$TPD profiles were attributed to the weak acidic/basic, moderate acidic/basic, and strong acidic/basic sites, respectively [30]. Studies have reported that weak basic sites are mainly ascribed to surface –OH groups, which react with $CO_2$ and form bicarbonates [31,32]. The moderate basic sites were derived from the Ce–$O_L$ or $O_V$–$O_L$ ion pairs, which combined with $CO_2$ and promoted the formation of bridged and bidentate carbonates [8,19,32], while the strong basic sites were mainly assigned to the low-coordination oxygen anions [8,31,32], which resulted in the formation of stable monodentate carbonates [33].

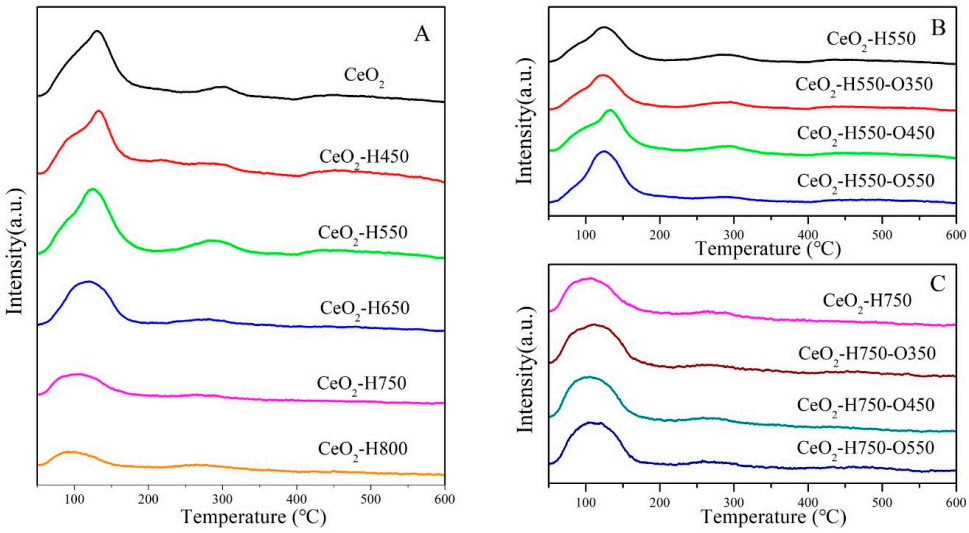



**Figure 6.** $NH_3$-TPD profiles of catalysts (**A**) $CeO_2$ reduced at different temperatures, (**B**) $CeO_2$–H550 reoxidized at different temperatures, and (**C**) $CeO_2$–H750 reoxidized at different temperatures.

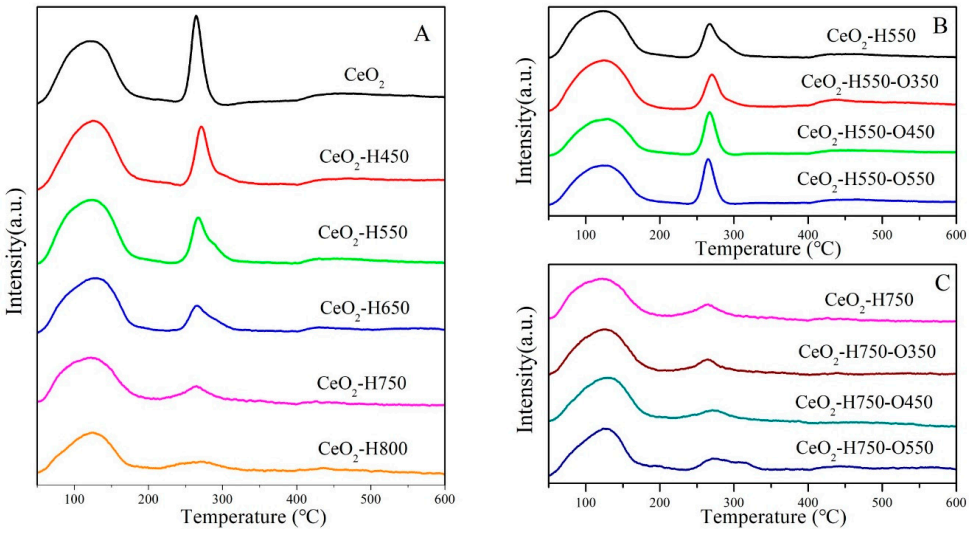



**Figure 7.** $CO_2$TPD profiles of catalysts (**A**) $CeO_2$ reduced at different temperatures, (**B**) $CeO_2$–H550 reoxidized at different temperatures, and (**C**) $CeO_2$–H750 reoxidized at different temperatures.

**Table 4.** Adsorption amount of $CO_2$ and $NH_3$ determined using TPD profiles.

| Catalysts | $CO_2$ Adsorption (mmol/g) | | | $NH_3$ Adsorption (mmol/g) | | |
|---|---|---|---|---|---|---|
| | Weak (<200 °C) | Moderate (200~400 °C) | Strong (>400 °C) | Weak (<200 °C) | Moderate (200~400 °C) | Strong (>400 °C) |
| $CeO_2$ | 0.607 | 0.206 | 0.039 | 0.592 | 0.158 | 0.040 |
| $CeO_2$–H450 | 0.533 | 0.147 | 0.025 | 0.472 | 0.124 | 0.046 |
| $CeO_2$–H550 | 0.525 | 0.136 | 0.020 | 0.586 | 0.134 | 0.043 |
| $CeO_2$–H650 | 0.361 | 0.074 | 0.015 | 0.384 | 0.084 | - |
| $CeO_2$–H750 | 0.142 | 0.023 | 0.002 | 0.199 | 0.018 | - |
| $CeO_2$–H800 | 0.113 | 0.019 | 0.006 | 0.117 | 0.031 | - |
| $CeO_2$–H550–O350 | 0.525 | 0.130 | 0.024 | 0.586 | 0.143 | 0.040 |
| $CeO_2$–H550–O450 | 0.538 | 0.154 | 0.028 | 0.416 | 0.143 | 0.037 |
| $CeO_2$–H550–O550 | 0.590 | 0.156 | 0.028 | 0.598 | 0.152 | 0.041 |
| $CeO_2$–H750–O350 | 0.183 | 0.023 | 0.004 | 0.227 | 0.022 | - |
| $CeO_2$–H750–O450 | 0.192 | 0.024 | 0.006 | 0.232 | 0.023 | - |
| $CeO_2$–H750–O550 | 0.205 | 0.039 | 0.007 | 0.240 | 0.027 | - |

Overall, the surface acidic sites with different natures all decreased with an increase in the reduction temperature and increased with an increase in the reoxidation temperature (Figure 6 and Table 4). A similar trend was observed for the surface basic sites under various treatment conditions (Figure 7 and Table 4). A possible reason for the change in surface acidity and basicity is discussed in Section 3.2.

### *2.6. Measurement of Catalytic Activity*

The DMC yields of $CeO_2$ treated under different conditions are displayed in Figure 8. As seen in Figure 8A, the DMC yield of $CeO_2$ gradually decreased from 9.02 to 1.75 mmol/g as the reduction temperature increased to 800 °C. However, as seen in Figure 8B,C, the DMC yield of $CeO_2$–H550 and $CeO_2$–H750 gradually increased from 6.94 and 2.85 to 7.98 and 4.21 mmol/g, respectively, as the reoxidation temperature increased to 550 °C. These results indicated that reduction treatment is detrimental to the improvement of catalytic activity but reoxidation treatment is beneficial.

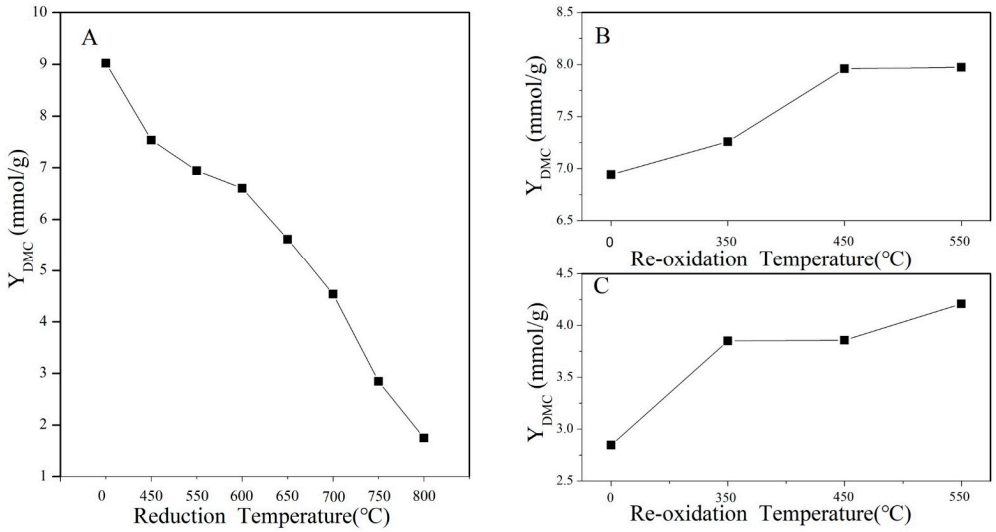



**Figure 8.** DMC yield of catalysts (**A**) $CeO_2$ reduced at different temperatures, (**B**) $CeO_2$–H550 reoxidized at different temperatures, and (**C**) $CeO_2$–H750 reoxidized at different temperatures.

## 3. Discussion

### *3.1. The Relationship between Catalytic Activity and Surface Acidity/Basicity*

Surface basicity and acidity play a significant role in determining the catalytic activity of $CeO_2$-based catalysts. Wang et al. [11] found that only bidentate carbonates can react with surface $–OCH_3$ originating from the dissociation of methanol and form MMC, which is considered an active intermediate species for the formation of DMC, while monodentate carbonates, bicarbonates, and bridged carbonates cannot accomplish this process. Inumaru et al. [34] also found that the catalytic activity of $ZrO_2$ nanocrystals is closely related to the surface bidentate carbonate species. As discussed in Section 2.4, bidentate carbonates were derived from the interaction of $CO_2$ with moderate basic sites. In addition, surface acidic sites significantly affected the adsorption and activation of methanol. Studies have reported that methanol is adsorbed and dissociated on acid sites and forms $–OCH_3$ groups, which participate in the formation of MMC [7,19,35]. Xiao et al. [8] revealed that catalytic activity is positively correlated with the moderate surface acidic/basic sites of Fe–Zr composite catalysts. Taking these findings into account, it is reasonable to build a relationship between catalytic activity and moderate surface acidic/basic sites. As shown in Figure 9A,B, catalytic activity was positively correlated with the number of moderate surface acid and basic sites (determined from $NH_3$-TPD and $CO_2$TPD profiles) of $CeO_2$ catalysts.

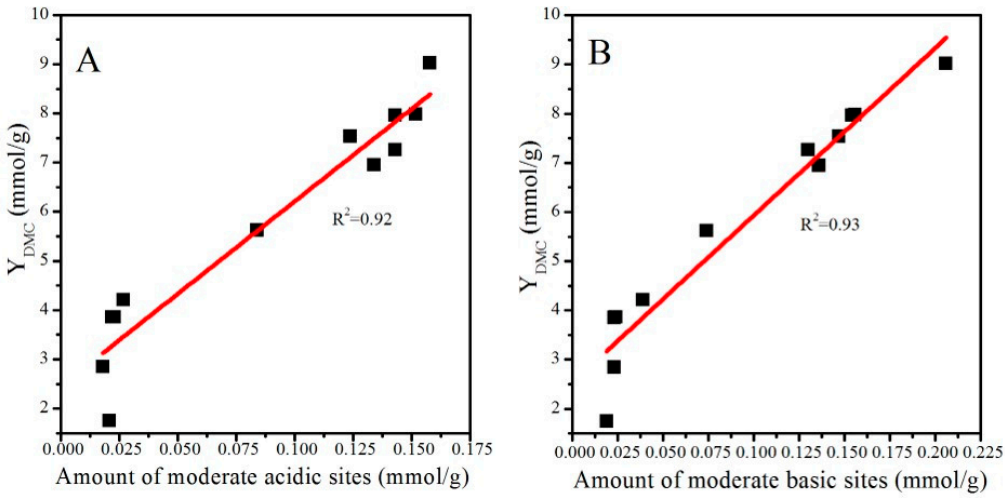



**Figure 9.** Relationships between catalytic activity and the number of moderate acidic (**A**) and basic (**B**) sites.

### *3.2. Deep Insight into the Role of $Ce^{4+}$ and $O_V$*

Marin et al. [9] reported that conversion of $CO_2$ and methanol to DMC over a $CeO_2$ catalyst follows a Langmuir–Hinshelwood mechanism, with the $CO_2$ adsorption step being rate controlling. However, there are two different theories about the adsorption and activation of $CO_2$ for $CeO_2$-based catalysts. One is that surface coordination unsaturated $Ce^{4+}$ ions and $O_L$ serve as Lewis acid–base pairs to promote the adsorption and activation of $CO_2$ [7,36,37]. The other is that surface $O_V$ and $O_L$ serve as Lewis acid–base pairs to promote the adsorption and activation of $CO_2$. Especially for metal-doped $CeO_2$ catalysts, it was found that one of the O atoms of $CO_2$ can be inserted into $O_V$ and thus promotes the adsorption and activation of $CO_2$, and therefore, the adsorption of $CO_2$ improves with an increase in surface $O_V$ [12,15,19]. Obviously, the focus was that of $Ce^{4+}$ or $O_V$, which Lewis acid sites determine the adsorption and activation of $CO_2$ for $CeO_2$ catalysts?

XPS results showed that reduction treatment results in a decrease in surface $Ce^{4+}$ and an increase in $O_V$. In contrast, reoxidation treatment resulted in a decrease in surface $O_V$ and an increase in $Ce^{4+}$. Combining XPS and $CO_2$-TPD results, it was apparent that the adsorption amount of $CO_2$ and the concentration of $Ce^{4+}$ showed a similar trend under various treatment conditions. Moreover, combining XPS and $NH_3$TPD results, we found

that the adsorption amount of $NH_3$ and the concentration of $Ce^{4+}$ shows a similar trend under various treatment conditions. These results indicated that surface $Ce^{4+}$ serves as active Lewis acid sites to adsorb and activate $CO_2$ and methanol molecules.

Nevertheless, it should be noted that the particle size of $CeO_2$ can also affect the adsorption of $CO_2$ and $NH_3$. For example, as the reduction temperature increased beyond 550 °C, the aggregation of $CeO_2$ particles occurred (Table 2 and Figure 3), which can also result in decreased adsorption of $CO_2$ and $NH_3$.

The profiles of the DMC yield for catalysts treated under different conditions with a change in the concentration of $Ce^{4+}$ and $O_V$ are presented in Figures 10 and 11, respectively.

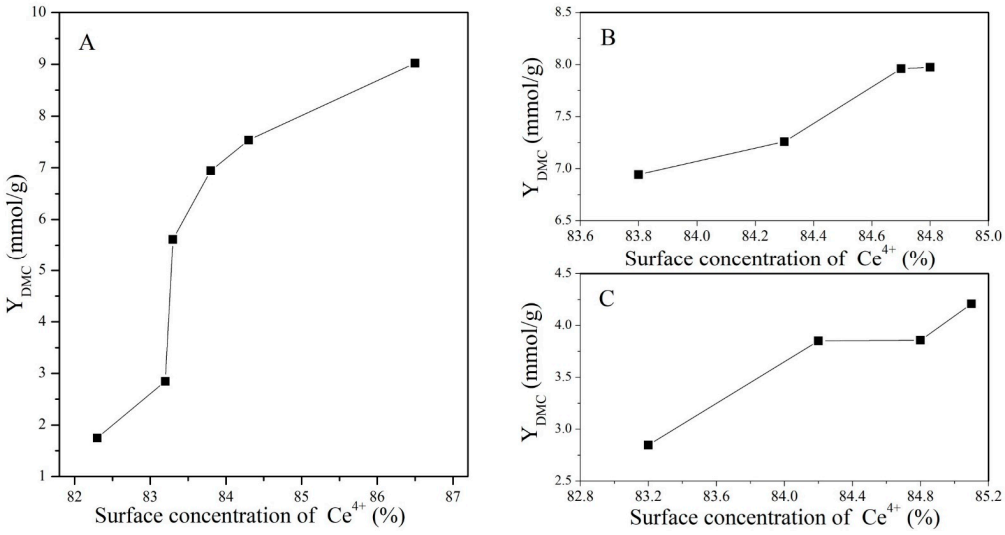



**Figure 10.** Variation in DMC yield with the surface concentration of $Ce^{4+}$: (**A**) $CeO_2$ reduced at different temperatures, (**B**) $CeO_2$–H550 reoxidized at different temperatures, and (**C**) $CeO_2$–H750 reoxidized at different temperatures.

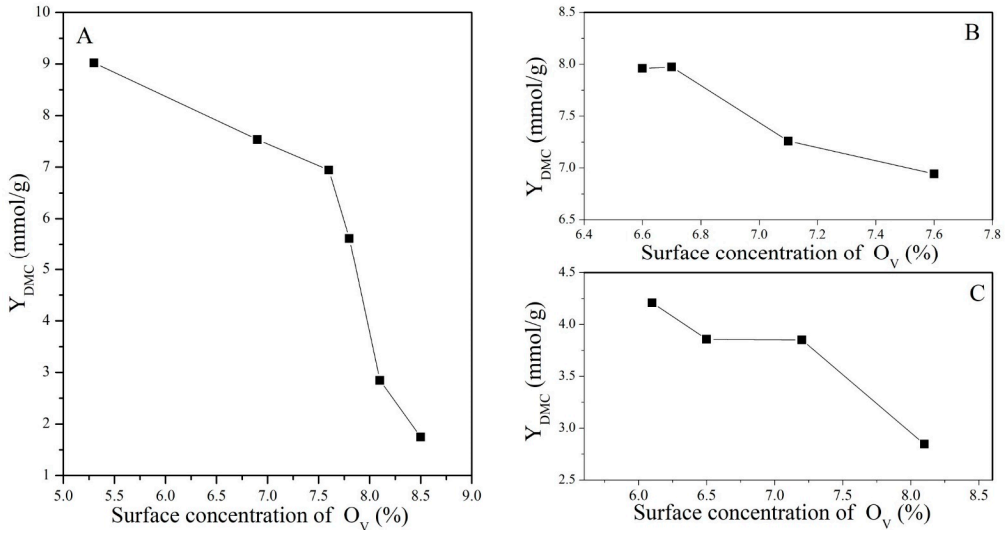



**Figure 11.** Variation in DMC yield with the surface concentration of $O_V$: (**A**) $CeO_2$ reduced at different temperatures, (**B**) $CeO_2$–H550 reoxidized at different temperatures, and (**C**) $CeO_2$–H750 reoxidized at different temperatures.

It was obvious that the catalytic activity increased with the increasing concentration of $Ce^{4+}$, while it decreased with the increasing concentration of $O_V$. Nevertheless, as discussed before, treatment conditions greatly affected the particle size of $CeO_2$, as presented in Table 2 and Figure 3. Generally, a particle with a smaller size is conducive to the exposure of more

active sites and thus improves the adsorption of the reactant and catalytic activity [38]. To eliminate the particle size effect, $CeO_2$, $CeO_2$–H450, $CeO_2$–H550, $CeO_2$–H550–O350, $CeO_2$–H550–O450, and $CeO_2$–H550–O550 catalysts (with similar crystal size of about 7~8 nm and basically an unchanged particle size) were selected to correlate the number of moderate basic sites as well as catalytic activity with the concentration of $Ce^{4+}$ and $O_V$. As shown in Figure 12, the number of moderate basic sites as well as catalytic activity were positively correlated with the concentration of surface $Ce^{4+}$ but negatively correlated with that of $O_V$.

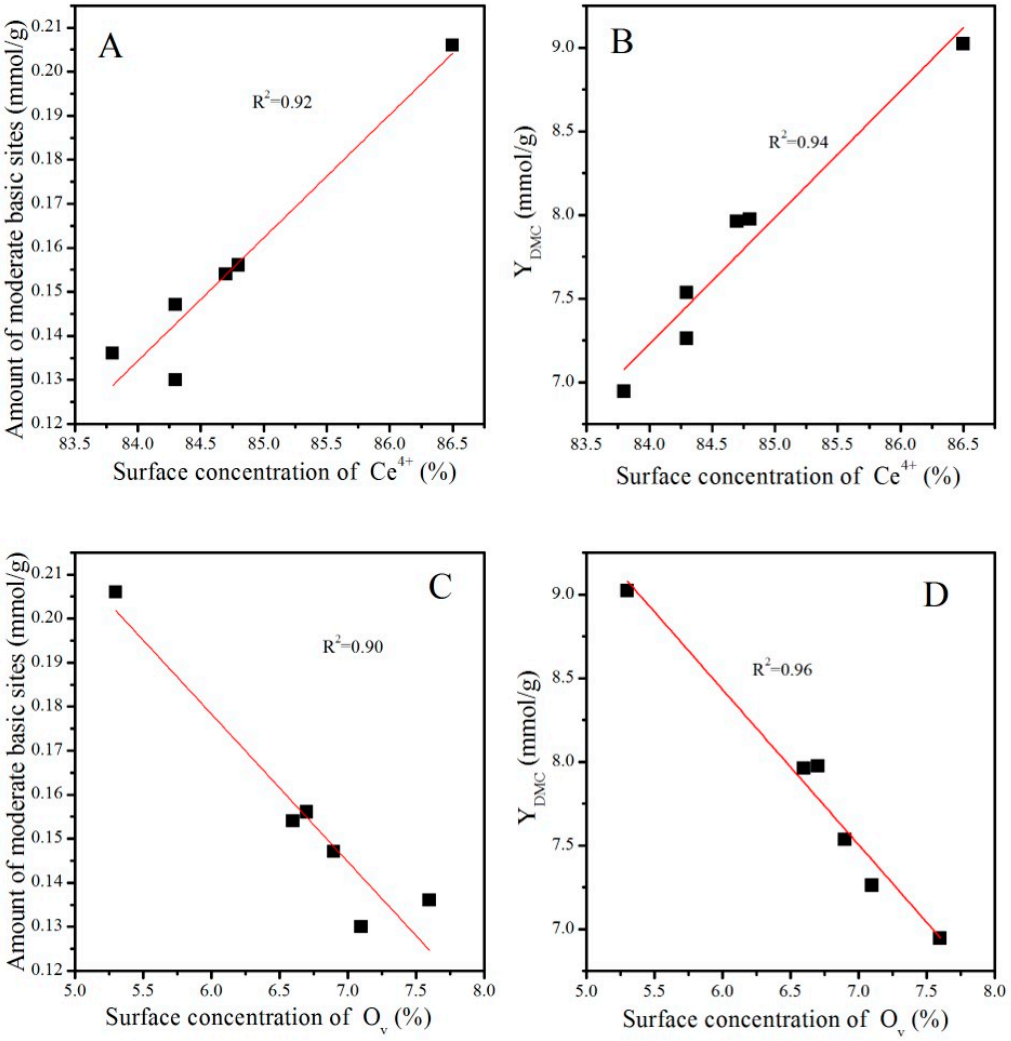



**Figure 12.** Correlations of the number of moderate basic sites and catalytic activity with the surface concentrations of $Ce^{4+}$ (**A**,**B**) and $O_V$ (**C**,**D**).

To further confirm the role of surface $Ce^{4+}$ in the formation of active bidentate carbonates, FTIR spectra of $CO_2$ adsorption for $CeO_2$, $CeO_2$–H550, and $CeO_2$–H550–O550 were developed, and the results are displayed in Figure 13. The bands at 1215, 1393, and 1610 $cm^{-1}$ were associated with bicarbonates, while the bands at 856, 1033, 1293, and 1581 $cm^{-1}$ were ascribed to bidentate carbonates [11,19]. In addition, the small bands at 1242 and 1652 $cm^{-1}$ were attributed to bridged carbonates, while the small bands at 1356 and 1466 $cm^{-1}$ were assigned to monodentate carbonates [11,19]. Obviously, the peak intensity and area of bidentate carbonates decreased after reduction treatment and increased after reoxidation treatment. These results strongly supported the fact that the surface $Ce^{4+}$ of $CeO_2$ serves as active Lewis acid sites and promotes the adsorption of $CO_2$ and the formation of bidentate carbonates and thus catalytic activity for the synthesis of DMC from $CO_2$ and methanol.

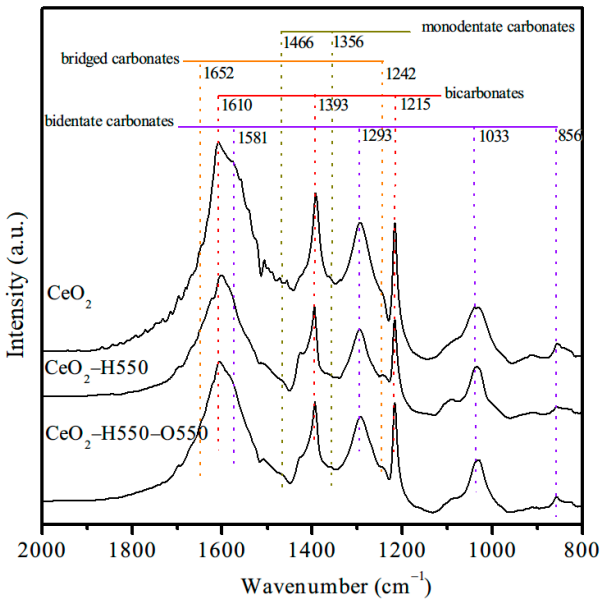



**Figure 13.** FTIR spectra of adsorbed $CO_2$ on $CeO_2$, $CeO_2$–H550, and $CeO_2$–H550–O550.

Why $O_V$ played an opposite role in the adsorption of $CO_2$ for pure $CeO_2$ and metal-doped $CeO_2$ catalytic systems is thought provoking. This may be because $O_V$ has a different nature in pure $CeO_2$ and metal-doped $CeO_2$ catalysts. As discussed in Section 2.3, the $O_V$ formed by $H_2$ reduction are a kind of anionic defect, and a material with this kind of defect is an N-type semiconductor [28]. The possible reason is that the quasi-free mobile electrons around $O_V$ impede the adsorption and activation of $CO_2$, and therefore, the catalytic activity decreases with an increase in $O_V$. This was consistent with the results reported by Tan et al. that the catalytic activity of $CeO_2$ prepared under different atmospheres follows the order $CeO_2$–$O_2$ > $CeO_2$–Ar > $CeO_2$–air > $CeO_2$–$H_2$; especially, the catalytic activity of $CeO_2$–$O_2$ was 2.5 times as high as that of $CeO_2$–$H_2$ [27]. However, for metal-doped $CeO_2$ catalysts, the $O_V$ derived from the incorporation of metal ions (for example, $Ca^{2+}$, $Zn^{2+}$, $Mn^{2+}$, $Ti^{4+}$, and $Zr^{4+}$) into the lattice of $CeO_2$ is a kind of cationic defect, and a material with this kind of defect is a P-type semiconductor[39,40]. This kind of cationic defect ($O_V$) is beneficial for the adsorption and activation of $CO_2$, and thus, the catalytic activity increases with an increase in $O_V$ [12,13,15,16,19]. The possible influence of two types of $O_V$ on the adsorption and activation of $CO_2$ is shown in Figure 14.

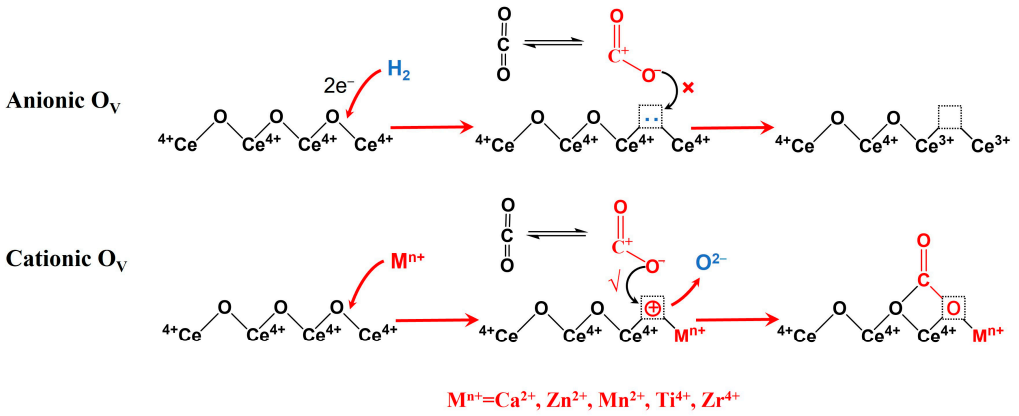



**Figure 14.** Possible influence of two types of $O_V$ on the adsorption and activation of $CO_2$.

It is interesting that similar phenomena have also been observed during the conversion of syngas to light olefins over $ZrCeZnO_x$ catalysts [41,42]. It was found that the

incorporation of $Ce^{3+}$ into Zn–Zr oxide improves the percentage of $O_V$ and thus catalytic activity [42]; however, the catalytic activity of $ZrCeZnO_x$ decreased after reduction with $H_2$, although the percentage of $O_V$ improved significantly [41]. This indicated that the types of $O_V$ remarkably affects the adsorption of CO and therefore catalytic activity.

## 4. Materials and Methods

### *4.1. Preparation of $CeO_2$*

First, 3.47 g of $Ce(NO_3)_3{\cdot}6H_2O$ was dissolved in 30 mL of deionized water. Next, 100 mL of NaOH solution (2 mol/L) was added to the solution of $Ce(NO_3)_3$ with a constant-flux pump under stirring. After aging for 1 h at ambient temperatures, the slurry was filtered and washed with deionized water and ethanol several times until it became neutral. Finally, the products were dried for 12 h at 80 °C and then calcinated for 5 h at 550 °C in a muffle furnace. The resultant catalyst was labeled as $CeO_2$ and used as a starting material for further treatment.

### *4.2. Reduction Treatment of $CeO_2$*

Typically, 0.25 g of $CeO_2$ was placed in a tube furnace, and then, the temperature was increased to 450, 550, 600, 650, 700, 750, and 800 °C under 10a % $H_2$–$N_2$ atmosphere for 4 h at a heating rate of 5 °C/min. The obtained catalysts were named as $CeO_2$–$HT_1$, where $T_1$ is the reduction temperature.

### *4.3. Reoxidation Treatment of $CeO_2$–H550 and $CeO_2$–H750*

Typically, 0.2 g of $CeO_2$–H550 or $CeO_2$–H750 was placed in a muffle furnace, and then, the temperature was increased to 350, 450 and 550 °C under an air atmosphere for 4 h at a heating rate of 2 °C/min. The obtained catalysts were named as $CeO_2$–H550–$OT_2$ or $CeO_2$–H750–$OT_2$, where $T_2$ is the reoxidation temperature.

### *4.4. Characterization of Supports and Catalysts*

$N_2$ physisorption was performed on a Beishide 3H-2000PS2 instrument at −196 °C using $N_2$ as an adsorbate. The sample was outgassed at 250 °C for 4 h in vacuum to remove the physisorbed impurities before measurement. The specific surface area and pore volume were calculated using the BET and BIH methods, respectively.

XRD characterization was carried out on a Rigaku SmartLab SE diffractometer (40 kV, 40 mA) with a diffraction angle ($2\theta$) from 10 to 80° and a scanning rate of 10°/min.

TEM images were taken with FEI Tecnai F30 at 200 kV. Before measurement, the sample was first dispersed in ethanol, then ultrasonicated for 30 min, and finally deposited on a carbon-coated copper film.

TPD characterization was performed on Micromeritics Autochem 2920. First, 100 mg of the sample was degassed for 30 min at 250 °C with $N_2$ (30 mL/min) to remove the physisorbed impurities. After the temperature was cooled down to 50 °C, 15% $NH_3$ in He (30 mL/min) or pure $CO_2$ (30 mL/min) was introduced and maintained for 30 min to allow saturated adsorption of $NH_3$ and $CO_2$. Subsequently, the physisorbed substance was removed with He (30 mL/min) at 50 °C for 30 min. Thereafter, the temperature was gradually increased to 800 °C at a heating rate of 10 °C/min with He as a carrier gas (30 mL/min), and the desorbed $NH_3$ and $CO_2$ were detected with TCD.

XPS spectra were analyzed with an ESCALAB 250Xi (Thermo Scientific, Waltham, MA, USA) photoelectron spectrometer under AlK$\alpha$ radiation at 300 W. The binding energies were referred to the C1s line from adventitious carbon at 284.6 eV.

$CO_2$-FTIR spectra were recorded using a Bruker Tensor II instrument equipped with an MCT detector by collecting 64 scans at a resolution of 4 $cm^{-1}$. About 20 mg of the sample was loaded into the cell and then pretreated under He flow (30 mL/min) at 400 °C for 1 h to remove the physisorbed impurities. After the temperature dropped down to 140 °C (reaction temperature), pure $CO_2$ (30 mL/min) was introduced and maintained for

30 min to allow saturated adsorption of $CO_2$. Subsequently, the physisorbed substance was removed with He (30 mL/min) for 30 min, and then, FTIR spectra were recorded.

### *4.5. Catalytic Evaluation*

The catalytic activity of catalysts for DMC synthesis from $CO_2$ and methanol was investigated in a 250 mL high-pressure slurry-bed reactor equipped with a mechanical stirrer. Typically, 0.2 g of a catalyst and 30 mL of methanol were placed into the reactor, which was subsequently sealed. Next, the reactor was filled with $CO_2$ several times to check the tightness and remove air. Thereafter, the reactor was pressurized with $CO_2$ to 3 MPa at ambient temperatures, and then, the reaction temperature was increased to 140 °C and maintained for 4 h. After the reaction finished, the reactor was depressurized and cooled down to room temperature. The liquid product was analyzed with n-propanol as an internal standard substance using a gas chromatograph (FID-GC, O Hua 9160). It should be noted that no by-products were formed except DMC, and the yield of DMC was defined as follows:

$$Y_{DMC}(\text{mmol/g}) = n_{DMC}(\text{mmol})/m_{catalyst}(\text{g}) \quad (1)$$

## 5. Conclusions

(1) The concentrations of surface $Ce^{4+}$ and oxygen vacancies of $CeO_2$ were regulated with reduction and reoxidation treatments under different conditions. The reduction treatment promoted the conversion of $Ce^{4+}$ to $Ce^{3+}$ and improved the surface concentration of oxygen vacancies, while the reoxidation treatment favored the conversion of $Ce^{3+}$ to $Ce^{4+}$ and decreased the concentration of oxygen vacancies.

(2) Catalytic activity was positively correlated with the number of moderate surface acidic/basic sites of catalysts. Moreover, the number of moderate basic sites and catalytic activity were positively correlated with the surface concentration of $Ce^{4+}$ but negatively correlated with that of oxygen vacancies.

(3) The surface $Ce^{4+}$ rather than oxygen vacancies served as active Lewis acid sites, and lattice oxygen served as active Lewis base sites to adsorb and activate $CO_2$, promoting the formation of active bidentate carbonates species and DMC.

(4) The cationic oxygen vacancy was beneficial but the anionic oxygen vacancy was detrimental to the formation of active bidentate carbonates species and DMC, which sheds light upon the active sites for $CeO_2$ and metal-doped $CeO_2$ catalysts and provides evidence for the design of efficient catalysts.

**Supplementary Materials:** The following supporting information can be downloaded at https://www.mdpi.com/article/10.3390/molecules28093785/s1, Figure S1: Change in the color of catalysts.

**Author Contributions:** Conceptualization, H.Z. and G.Z.; methodology, Y.Z.; software, S.Z.; formal analysis, Y.S.; investigation, Y.Y. and T.K.; data curation, G.Z.; writing—review and editing, G.Z. and H.Z.; supervision, H.Z.; funding acquisition, H.Z. and G.Z. All authors have read and agreed to the published version of the manuscript.

**Funding:** This research was funded by the National Natural Science Foundation of China (22262020); the Guizhou Provincial Basic Research Program (Natural Science; ZK[2023]YB448 and ZK[2023]YB447); the Zunyi Technology and Big data Bureau, Moutai Institute Joint Science and Technology Research and Development Project ([2021]328); and the Research Foundation for Scientific Scholars of Moutai Institute (mygccrc [2022]080 and [2022]081).

**Data Availability Statement:** All the relevant data used in this study have been provided in the form of figures and tables in the published article, and all data provided in the manuscript are available to whom they may concern.

**Acknowledgments:** The authors are grateful to Zhong Li, Nilesh Narkhede, and Yuchen Sun for their kind academic discussion and language help.

**Conflicts of Interest:** The authors declare no conflict of interest.

## References


1. Jiang, X.; Nie, X.; Guo, X.; Song, C.; Chen, J.G. Recent Advances in Carbon Dioxide Hydrogenation to Methanol via Heterogeneous Catalysis. *Chem. Rev.* **2020**, *120*, 7984–8034. [CrossRef] [PubMed]
2. Rogelj, J.; Huppmann, D.; Krey, V.; Riahi, K.; Clarke, L.; Gidden, M.; Nicholls, Z.; Meinshausen, M. A new scenario logic for the Paris Agreement long-term temperature goal. *Nature* **2019**, *573*, 357–363. [CrossRef] [PubMed]
3. Huang, S.; Yan, B.; Wang, S.; Ma, X. Recent advances in dialkyl carbonates synthesis and applications. *Chem. Soc. Rev.* **2015**, *44*, 3079–3116. [CrossRef]
4. Zhang, M.; Xu, Y.; Williams, B.L.; Xiao, M.; Wang, S.; Han, D.; Sun, L.; Meng, Y. Catalytic materials for direct synthesis of dimethyl carbonate (DMC) from $CO_2$. *J. Clean. Prod.* **2021**, *279*, 123344. [CrossRef]
5. Tamboli, A.H.; Chaugule, A.A.; Kim, H. Catalytic developments in the direct dimethyl carbonate synthesis from carbon dioxide and methanol. *Chem. Eng. J.* **2017**, *323*, 530–544. [CrossRef]
6. Tomishige, K.; Sakaihori, T.; Ikeda, Y.; Fujimoto, K. A novel method of direct synthesis of dimethyl carbonate from methanol and carbon dioxide catalyzed by zirconia. *Catal. Lett.* **1999**, *58*, 225–229. [CrossRef]
7. Jung, K.T.; Bell, A.T. An in Situ Infrared Study of Dimethyl Carbonate Synthesis from Carbon Dioxide and Methanol over Zirconia. *J. Catal.* **2001**, *204*, 339–347. [CrossRef]
8. Li, A.; Pu, Y.; Li, F.; Luo, J.; Zhao, N.; Xiao, F. Synthesis of dimethyl carbonate from methanol and $CO_2$ over Fe-Zr mixed oxides. *J. CO2 Util.* **2017**, *19*, 33–39. [CrossRef]
9. Marin, C.M.; Li, L.; Bhalkikar, A.; Doyle, J.E.; Zeng, X.C.; Cheung, C.L. Kinetic and mechanistic investigations of the direct synthesis of dimethyl carbonate from carbon dioxide over ceria nanorod catalysts. *J. Catal.* **2016**, *340*, 295–301. [CrossRef]
10. Wang, S.-P.; Zhou, J.-J.; Zhao, S.-Y.; Zhao, Y.-J.; Ma, X.-B. Enhancements of dimethyl carbonate synthesis from methanol and carbon dioxide: The in situ hydrolysis of 2-cyanopyridine and crystal face effect of ceria. *Chin. Chem. Lett.* **2015**, *26*, 1096–1100. [CrossRef]
11. Zhao, S.-Y.; Wang, S.-P.; Zhao, Y.-J.; Ma, X.-B. An in situ infrared study of dimethyl carbonate synthesis from carbon dioxide and methanol over well-shaped $CeO_2$. *Chin. Chem. Lett.* **2017**, *28*, 65–69. [CrossRef]
12. Liu, B.; Li, C.M.; Zhang, G.Q.; Yan, L.F.; Li, Z. Direct synthesis of dimethyl carbonate from $CO_2$ and methanol over CaO-$CeO_2$ catalysts: The role of acid-base properties and surface oxygen vacancies. *New J. Chem.* **2017**, *41*, 12231–12240. [CrossRef]
13. Chen, Y.; Tang, Q.; Ye, Z.; Li, Y.; Yang, Y.; Pu, H.; Li, G. Monolithic $Zn_xCe_{1-x}O_2$ catalysts for catalytic synthesis of dimethyl carbonate from $CO_2$ and methanol. *New J. Chem.* **2020**, *44*, 12522–12530. [CrossRef]
14. Liu, N.; Xue, Y.; Yu, Z.R.; Li, Y.Y.; Xu, Y.; Xu, J.; Xue, B.; Luo, J.; Wang, F. Zn-Doped $CeO_2$ Nanorods: A Highly Efficient Heterogeneous Catalyst for the Direct Synthesis of Dimethyl Carbonate from $CO_2$ and Methanol. *Chemistryselect* **2023**, *8*, e202203472. [CrossRef]
15. Zhang, G.; Sun, Y.; Shi, Y.; Zheng, H.; Li, Z.; Ju, S.; Liu, S.; Shi, P. Surface Properties of $Ce_{1-x}Mn_xO_2$ Catalyst on the Catalytic Activities for Direct Synthesis of DMC from $CO_2$ and Methanol. *Chem. J. Chin. Univ.* **2020**, *41*, 2061–2069.
16. Chen, Y.; Wang, H.; Qin, Z.; Tian, S.; Ye, Z.; Ye, L.; Abroshan, H.; Li, G. $Ti_xCe_{1-x}O_2$ nanocomposites: A monolithic catalyst for the direct conversion of carbon dioxide and methanol to dimethyl carbonate. *Green Chem.* **2019**, *21*, 4642–4649. [CrossRef]
17. Luo, M.S.; Qin, T.; Liu, Q.L.; Yang, Z.; Wang, F.L.; Li, H. Novel Fe-modified $CeO_2$ Nanorod Catalyst for the Dimethyl Carbonate Formation from $CO_2$ and Methanol. *ChemCatChem* **2022**, *14*, e202200253. [CrossRef]
18. Kulal, N.; Bhat, S.S.; Hugar, V.; Mallannavar, C.N.; Lee, S.C.; Bhattacharjee, S.; Vetrivel, R.; Shanbhag, G.V. Integrated DFT and experimental study on $Co_3O_4/CeO_2$ catalyst for direct synthesis of dimethyl carbonate from $CO_2$. *J. CO2 Util.* **2023**, *67*, 102323. [CrossRef]
19. Liu, B.; Li, C.M.; Zhang, G.Q.; Yao, X.S.; Chuang, S.S.C.; Li, Z. Oxygen Vacancy Promoting Dimethyl Carbonate Synthesis from $CO_2$ and Methanol over Zr-Doped $CeO_2$ Nanorods. *ACS Catal.* **2018**, *8*, 10446–10456. [CrossRef]
20. Xu, S.Y.; Cao, Y.X.; Liu, Z.M. Dimethyl carbonate synthesis from $CO_2$ and methanol over $CeO_2$-$ZrO_2$ catalyst. *Catal. Commun.* **2022**, *162*, 106397. [CrossRef]
21. Giordano, F.; Trovarelli, A.; de Leitenburg, C.; Giona, M. A Model for the Temperature-Programmed Reduction of Low and High Surface Area Ceria. *J. Catal.* **2000**, *193*, 273–282. [CrossRef]
22. Hezam, A.; Namratha, K.; Drmosh, Q.A.; Ponnamma, D.; Wang, J.W.; Prasad, S.; Ahamed, M.; Cheng, C.; Byrappa, K. $CeO_2$ Nanostructures Enriched with Oxygen Vacancies for Photocatalytic $CO_2$ Reduction. *ACS Appl. Nano Mater.* **2020**, *3*, 138–148. [CrossRef]
23. Yoshida, Y.; Arai, Y.; Kado, S.; Kunimori, K.; Tomishige, K. Direct synthesis of organic carbonates from the reaction of $CO_2$ with methanol and ethanol over $CeO_2$ catalysts. *Catal. Today* **2006**, *115*, 95–101. [CrossRef]
24. Aneggi, E.; Wiater, D.; de Leitenburg, C.; Llorca, J.; Trovarelli, A. Shape-Dependent Activity of Ceria in Soot Combustion. *ACS Catal.* **2014**, *4*, 172–181. [CrossRef]
25. Wang, X.; Jiang, Z.Y.; Zheng, B.J.; Xie, Z.X.; Zheng, L.S. Synthesis and shape-dependent catalytic properties of $CeO_2$ nanocubes and truncated octahedra. *Crystengcomm* **2012**, *14*, 7579–7582. [CrossRef]
26. Swiatowska, J.; Lair, V.; Pereira-Nabais, C.; Cote, G.; Marcus, P.; Chagnes, A. XPS, XRD and SEM characterization of a thin ceria layer deposited onto graphite electrode for application in lithium-ion batteries. *Appl. Surf. Sci.* **2011**, *257*, 9110–9119. [CrossRef]
27. Cui, Z.; Fan, J.; Duan, H.; Zhang, J.; Xue, Y.; Tan, Y. Effect of calcination atmospheres on the catalytic performance of nano-$CeO_2$ in direct synthesis of DMC from methanol and $CO_2$. *Korean J. Chem. Eng.* **2017**, *34*, 29–36. [CrossRef]

28. Xing, Y.M.; Wu, Y.; Li, L.Y.; Shi, Q.; Shi, J.; Yun, S.N.; Akbar, M.; Wang, B.Y.; Kim, J.S.; Zhu, B. Proton Shuttles in $CeO_2$/$CeO_2$-delta Core-Shell Structure. *ACS Energy Lett.* **2019**, *4*, 2601–2607. [CrossRef]
29. Singhal, R.K.; Kumar, S.; Samariya, A.; Dhawan, M.; Sharma, S.C.; Xing, Y.T. Investigating the mechanism of ferromagnetic exchange interaction in non-doped $CeO_2$ with regard to defects and electronic structure. *Mater. Chem. Phys.* **2012**, *132*, 534–539. [CrossRef]
30. Liu, H.; Zou, W.; Xu, X.; Zhang, X.; Yang, Y.; Yue, H.; Yu, Y.; Tian, G.; Feng, S. The proportion of $Ce^{4+}$ in surface of $Ce_xZr_{1-x}O_2$ catalysts: The key parameter for direct carboxylation of methanol to dimethyl carbonate. *J. CO2 Util.* **2017**, *17*, 43–49. [CrossRef]
31. Kumar, P.; Srivastava, V.C.; Glaeser, R.; With, P.; Mishra, I.M. Active ceria-calcium oxide catalysts for dimethyl carbonate synthesis by conversion of $CO_2$. *Powder Technol.* **2017**, *309*, 13–21. [CrossRef]
32. Leino, E.; Kumar, N.; Mäki-Arvela, P.; Rautio, A.-R.; Dahl, J.; Roine, J.; Mikkola, J.-P. Synthesis and characterization of ceria-supported catalysts for carbon dioxide transformation to diethyl carbonate. *Catal. Today* **2018**, *306*, 128–137. [CrossRef]
33. Kumar, P.; With, P.; Srivastava, V.C.; Shukla, K.; Glaser, R.; Mishra, I.M. Dimethyl carbonate synthesis from carbon dioxide using ceria-zirconia catalysts prepared using a templating method: Characterization, parametric optimization and chemical equilibrium modeling. *RSC Adv.* **2016**, *6*, 110235–110246. [CrossRef]
34. Akune, T.; Morita, Y.; Shirakawa, S.; Katagiri, K.; Inumaru, K. $ZrO_2$ Nanocrystals As Catalyst for Synthesis of Dimethylcarbonate from Methanol and Carbon Dioxide: Catalytic Activity and Elucidation of Active Sites. *Langmuir* **2018**, *34*, 23–29. [CrossRef]
35. Tomishige, K.; Ikeda, Y.; Sakaihori, T.; Fujimoto, K. Catalytic properties and structure of zirconia catalysts for direct synthesis of dimethyl carbonate from methanol and carbon dioxide. *J. Catal.* **2000**, *192*, 355–362. [CrossRef]
36. Fan, H.-X.; Feng, J.; Li, W.-Y.; Li, X.-H.; Wiltowski, T.; Ge, Q.-F. Role of $CO_2$ in the oxy-dehydrogenation of ethylbenzene to styrene on the $CeO_2$(111) surface. *Appl. Surf. Sci.* **2018**, *427*, 973–980. [CrossRef]
37. Lu, X.Q.; Wang, W.L.; Wei, S.X.; Guo, C.; Shao, Y.; Zhang, M.M.; Deng, Z.G.; Zhu, H.Y.; Guo, W.Y. Initial reduction of $CO_2$ on perfect and O-defective $CeO_2$ (111) surfaces: Towards CO or COOH? *RSC Adv.* **2015**, *5*, 97528–97535. [CrossRef]
38. Bell, A.T. The Impact of Nanoscience on Heterogeneous Catalysis. *Science* **2003**, *299*, 1688–1691. [CrossRef]
39. Schmale, K.; Daniels, M.; Buchheit, A.; Grunebaum, M.; Haase, L.; Koops, S.; Wiemhofer, H.D. Influence of Zinc Oxide on the Conductivity of Ceria. *J. Electrochem. Soc.* **2013**, *160*, F1081–F1087. [CrossRef]
40. Buchheit, A.; Tessmer, B.; Ran, K.; Mayer, J.; Wiemofer, H.D.; Neuhaus, K. The Impact of Fe Addition on the Electronic Conductivity of Gadolinium Doped Ceria. *ECS J. Solid. State Sci. Technol.* **2019**, *8*, P41–P50. [CrossRef]
41. Meng, F.H.; Li, X.J.; Zhang, P.; Yang, L.L.; Liu, S.S.; Li, Z. A facile approach for fabricating highly active $ZrCeZnO_x$ in combination with SAPO-34 for the conversion of syngas into light olefins. *Appl. Surf. Sci.* **2021**, *542*, 148713. [CrossRef]
42. Meng, F.H.; Li, X.J.; Zhang, P.; Yang, L.L.; Yang, G.N.; Ma, P.C.; Li, Z. Highly active ternary oxide $ZrCeZnO_x$ combined with SAPO-34 zeolite for direct conversion of syngas into light olefins. *Catal. Today* **2021**, *368*, 118–125. [CrossRef]


**Disclaimer/Publisher's Note:** The statements, opinions and data contained in all publications are solely those of the individual author(s) and contributor(s) and not of MDPI and/or the editor(s). MDPI and/or the editor(s) disclaim responsibility for any injury to people or property resulting from any ideas, methods, instructions or products referred to in the content.